


## ARTICLE OPEN



# Amplitude and frequency sensing of microwave fields with a superconducting transmon qudit

M. Kristen<sup>1</sup>✉, A. Schneider<sup>1</sup> , A. Stehli<sup>1</sup>, T. Wolz<sup>1</sup> , S. Danilin<sup>1</sup> , H. S. Ku<sup>3</sup>, J. Long<sup>3</sup>, X. Wu<sup>3</sup>, R. Lake<sup>3</sup>, D. P. Pappas<sup>3</sup>, A. V. Ustinov<sup>1,4</sup> and M. Weides<sup>1,2</sup> 

Experiments with superconducting circuits require careful calibration of the applied pulses and fields over a large frequency range. This remains an ongoing challenge as commercial semiconductor electronics are not able to probe signals arriving at the chip due to its cryogenic environment. Here, we demonstrate how the on-chip amplitude and frequency of a microwave signal can be inferred from the ac Stark shifts of higher transmon levels. In our time-resolved measurements we employ Ramsey fringes, allowing us to detect the amplitude of the systems transfer function over a range of several hundreds of MHz with an energy sensitivity on the order of  $10^{-4}$ . Combined with similar measurements for the phase of the transfer function, our sensing method can facilitate pulse correction for high fidelity quantum gates in superconducting circuits. Additionally, the potential to characterize arbitrary microwave fields promotes applications in related areas of research, such as quantum optics or hybrid microwave systems including photonic, mechanical or magnonic subsystems.

npj Quantum Information (2020)6:57; <https://doi.org/10.1038/s41534-020-00287-w>

## INTRODUCTION

Implementing a fault-tolerant quantum processor requires gate fidelities far exceeding a threshold of 99%<sup>1–4</sup>. In superconducting qubits, these gates are realized by on or near-resonant microwave pulses<sup>5</sup>. However, on the way to the circuit, the shape of these pulses is distorted by multiple passive microwave components such as attenuators, circulators and wires. These distortions negatively affect the gate fidelities if they are not accounted for.

The collective response of all microwave components to an incident signal is described by the transfer function of the system. If the transfer function is known, digital signal processing techniques allow for full control over the shape of applied pulses. However, since superconducting circuits are embedded in a cryogenic environment operated at millikelvin temperatures, the transfer function from pulse source to sample is not accessible with conventional network analyzers. In the past, this problem has been tackled by different calibration methods, which are usually limited to specific pulse shapes<sup>6</sup> or systems<sup>7</sup>. While more general pulse optimization schemes have been proposed theoretically, they have yet to be implemented in a real quantum system<sup>8–10</sup>.

In recent years, the growing interest in quantum sensors<sup>11–13</sup> has facilitated a more direct approach, where the signal arriving at the circuit is probed directly. In particular, superconducting qubits have been successfully employed as photon sensors due to their high electrical dipole moment. While sensing based on a variety of physical phenomena such as the cross-Kerr effect<sup>14</sup>, occurrence of the Mollow triplet<sup>15</sup> or electromagnetically induced transparency<sup>16</sup> has been shown, these methods are limited to the discrete frequencies of the qubit transitions. An alternative approach operates a qubit as a vector network analyzer, but only works in the MHz regime<sup>17</sup>. Recently, Schneider et al. demonstrated that the ac Stark effect in anharmonic multi-level quantum systems (qudit) can be used to detect on-chip microwave fields<sup>18</sup>. Here, signals over a range of more than one GHz were measured. When

including higher levels<sup>19</sup>, this sensor can simultaneously determine the amplitude and frequency of an unknown signal, promoting it as a useful tool for experiments in quantum optics<sup>20–22</sup> and quantum microwave photonics<sup>23–25</sup>, where in-situ frequency detection can be beneficial. However, the spectroscopic measurement techniques employed in these proof of principle experiments offer limited precision for reasonable data acquisition times.

In this work, we investigate the potential of the type of sensor used in ref. <sup>18</sup> to characterize the microwave transmission from source to sample. We use a time-resolved measurement setup to boost the sensor performance by an order of magnitude. By applying a well known microwave signal, we probe the amplitude of the transfer function over a wide frequency range. Finally, we estimate the errors and limits of our sensing scheme and discuss the potential for further improvement.

## RESULTS

The sensor we use in our experiments is a non-tunable superconducting transmon ( $\omega_J/2\pi = 4.685$  GHz) with a concentric design<sup>26</sup>. The transmon architecture offers a low anharmonicity (280 MHz), which is beneficial for probing higher qudit transitions, as well as an enhanced dipole moment, which increases the sensitivity to local ac fields<sup>27</sup>. To allow for manipulation ( $P_G$ ,  $\omega_G$ ) and readout (via a resonator) of the qudit, the sample is connected to a time resolved measurement setup (Fig. 1a). An additional microwave source with frequency  $\omega_F$  and power  $P_F$  was installed to generate a on-chip field with amplitude  $A_F \propto \sqrt{10^{P_F/10\text{dBm}}}$ . Neglecting the readout resonator, the Hamiltonian describing our system reads

$$H/\hbar = \sum_i \frac{\epsilon_i}{\hbar} |i\rangle\langle i| + A_G(t)(\hat{b} + \hat{b}^\dagger) \cos \omega_G t + A_F(\hat{b} + \hat{b}^\dagger) \cos \omega_F t, \quad (1)$$

<sup>1</sup>Institute of Physics, Karlsruhe Institute of Technology, 76131 Karlsruhe, Germany. <sup>2</sup>James Watt School of Engineering, University of Glasgow, Glasgow G12 8LT, UK. <sup>3</sup>National Institute of Standards and Technology, Boulder, CO 80309, USA. <sup>4</sup>Russian Quantum Center, National University of Science and Technology MISIS, 119049 Moscow, Russia. ✉email: [maximilian.kristen@kit.edu](mailto:maximilian.kristen@kit.edu); [martin.weides@glasgow.ac.uk](mailto:martin.weides@glasgow.ac.uk)

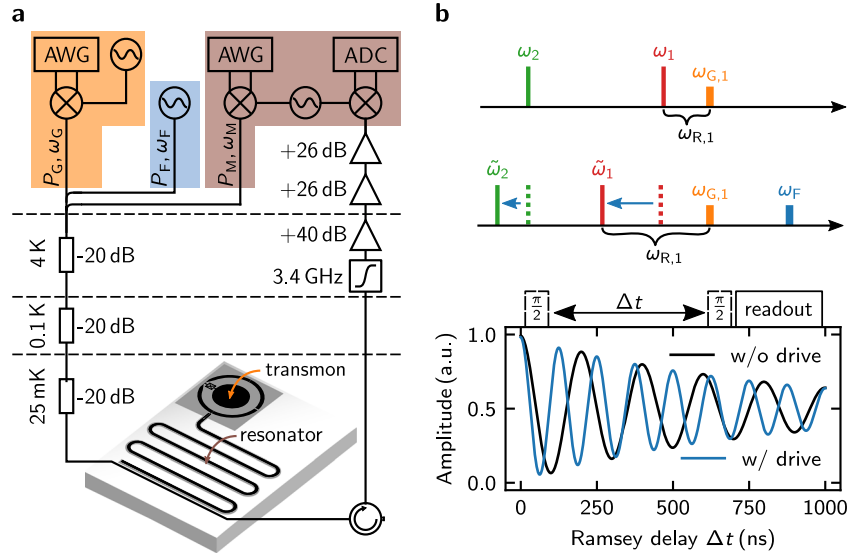


**Fig. 1 Experimental setup and methods.** **a** Schematic diagram of the transmon qudit sensor and readout resonator (coplanar waveguide) connected to the employed microwave setup. The gate ( $P_G, \omega_G$ ) and readout ( $P_M, \omega_M$ ) pulses are merged with the continuous tone ( $P_F, \omega_F$ ) which creates the on-chip microwave field to be measured. The combined signals are repeatedly attenuated within the cryostat before reaching the sample mounted at the 25 mK stage. **b** Graphical representation of the sensor measurement procedure. As the qudit transitions  $\omega_i$  ( $i = 1, 2$ ) are shifted in the presence of a microwave field, the frequency  $\omega_{R,i}$  of the corresponding Ramsey oscillations changes, here exemplified for  $\omega_1$ . Ramsey fringes thus reveal the magnitude of these level shifts. Together, the shifts of the first two qudit levels can be used to extract the amplitude and frequency of the microwave field.

where the anharmonic annihilation and creation operators  $\hat{b}$  and  $\hat{b}^\dagger$  take the different coupling strengths to the transmon levels into account, which are expressed in their Eigenbasis  $|i\rangle$ . The Eigenenergies  $E_i$  are calculated from the exact solution of the Transmon Hamiltonian<sup>27</sup>. In the following, we label the qudit transitions  $\omega_i = E_i - E_{i-1}$  and their associated parameters with identical indices.

To detect the amplitude and frequency of an on-chip microwave field we determine the ac Stark shift  $\Delta_i$  that it induces in the first and second qudit transition ( $i = 1, 2$ ). A simple but precise way to measure those shifts are Ramsey fringes<sup>28,29</sup>. The overall idea of the measurement scheme is sketched in Fig. 1b. Generally, performing Ramsey interferometry for a specific transition produces oscillations in the population of the associated qudit states. In the absence of an external field, the frequency of these oscillations simply depends on the frequency mismatch between the respective qudit transition and the applied gate tone  $\omega_{G,i}$ . However, if the qudit is subjected to a microwave field, this mismatch changes due to the ac Stark effect. The shift of any qudit transition

$$\Delta_i = \omega_{R,i} - (\omega_{G,i} - \omega_i), \quad (2)$$

can then be calculated from the oscillation frequency  $\omega_{R,i}$  corresponding to the respective Ramsey fringes, as long as the unperturbed qudit frequencies  $\omega_i$  are known.

Figure 2 shows Ramsey oscillations of the first and second qudit transition when applying a field with  $\omega_{F,apl}/2\pi = 5.285$  GHz and  $P_{F,apl} = 4$  dBm. In the experiments, a  $\pi$ -pulse prior to the Ramsey sequence allows probing the frequency shift of the second excited state. An identical  $\pi$ -pulse after the sequence increases the visibility and removes the spurious signal of the relaxation to the ground state. For these  $\pi$ -pulses to be on resonance with the shifted transition frequency  $\tilde{\omega}_1 = \omega_1 - \Delta_1$ , knowledge of  $\Delta_1$  is required. Consequently, the order in which the qudit transitions are probed is fixed. To determine the frequencies of the Ramsey oscillations, we fit the data with an exponentially damped sine function, which also accounts for the additional decay channels of higher lying qudit levels<sup>30</sup> via a declining amplitude offset. This

decay of the higher excited level also limits the maximum Ramsey delay time  $\Delta t$  used in our experiments (see Supplementary Information for details).

Lacking a closed analytical solution, the ac Stark shifts  $\Delta_i$  calculated from  $\omega_{R,i}$  are then evaluated with a pair of lookup tables. Each lookup table contains the expected shifts of the respective qudit transition for various microwave fields. Searching both lookup tables simultaneously for the entries that are closest to our measurement data yields an unambiguous result for the frequency and amplitude of the detected field. In ref.<sup>18</sup>, these lookup tables are generated analytically by modeling the transmon as an anharmonic oscillator. The field dependent level shifts are then calculated from perturbation theory. However, we find that this simplified model is no longer accurate when detecting frequency shifts with a precision of a few kilohertz. We therefore rely on numerical simulations of the exact transmon Hamiltonian (Eq. (1), see Methods for details).

The last plot in Fig. 2 shows the numerically generated lookup table for the first qudit transition, illustrating the dependency of the ac Stark shift on the amplitude and frequency of the microwave field. Here, a black and white line represent the upper and lower limit of the sensor, respectively. These limits originate from the restricted number of measurement points for the Ramsey fringes and will be discussed in detail later. Evaluating the data in Fig. 2 we find microwave photons of frequency  $\omega_{F,ex}/2\pi = 5.297$  GHz arriving at the qudit at a rate of  $A_{F,ex}/2\pi = 0.097$  GHz, which corresponds to a power of  $P_{F,ex} = A_{F,ex}\hbar\omega_{F,ex} = -116.7$  dBm.

The full sensing scheme proposed in this work can be summarized as a three step process. After measuring the shift of the first and second qudit transition using Ramsey fringes, the field parameters are extracted from the measurement data with the help of pre-calculated lookup tables. To verify the scheme, we apply a well known microwave signal with constant power and gradually increase the frequency over a range of 450 MHz. We probe the field arriving on-chip with our sensor and plot the extracted  $\omega_{F,ex}$  over the applied frequencies  $\omega_{F,apl}$  (Fig. 3a), finding a good agreement. Plotting  $A_{F,ex}$  over the same axis yields the amplitude of the transfer function (Fig. 3c). Here, we observe a strong frequency dependence, dominated by the readout

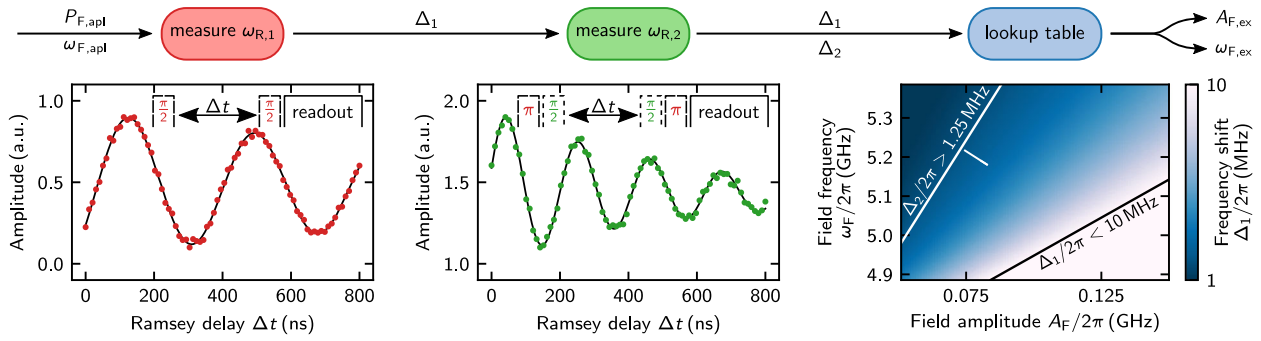


**Fig. 2 Employed sensing scheme.** First, the shift of the first qudit transition  $\Delta_1$  is determined from the frequency of the corresponding Ramsey oscillations. Second,  $\Delta_1$  is used to adjust the resonant  $\pi$ -pulse which excites the qudit to the  $|1\rangle$  state. Then, an additional Ramsey experiment is performed between  $|1\rangle$  and  $|2\rangle$  measuring  $\Delta_2$ . Third,  $\Delta_1$  and  $\Delta_2$  are processed by a pair of lookup tables to determine the frequency and amplitude of the microwave field causing the shifts. Here, only the lookup table for  $\Delta_1$  is shown. The sensor limits depicted within the lookup table are derived in the main section.

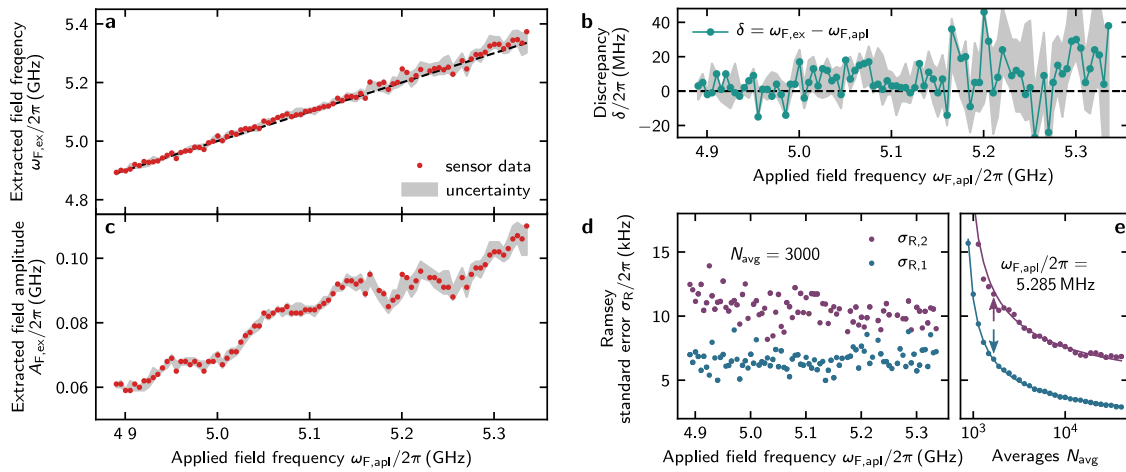


**Fig. 3 Sensor performance analysis.** **a** Comparison between the frequencies applied with the microwave source ( $\omega_{F,apl}$ ) and the frequencies extracted from the sensor ( $\omega_{F,ex}$ ). The shaded area indicates the uncertainty estimated from the standard errors to the Ramsey fits. **b** The magnitude of the discrepancy between  $\omega_{F,ex}$  and  $\omega_{F,apl}$  is an indicator for the reliability of our measurements. **c** Amplitude of our measurements. **d** Ramsey standard errors used for the calculation of the uncertainty in **a** and **c**. The values are extracted from the same fits as the sensor data. **e** Standard errors as a function of the number of averages. For this experiment,  $N_{avg} = 3000$  averages were used (indicated by the arrows).

resonator operating as a filter and cable resonances, which demonstrates the significance of calibrating microwave lines.

Shaded areas in Fig. 3 illustrate the uncertainty of our results. The uncertainty is estimated from varying our experimentally determined value of  $\Delta_i$  by  $\pm\sigma_{R,i}$  where  $\sigma_{R,i}$  is the standard error of  $\omega_{R,i}$  resulting from the fit. In our case,  $\sigma_{R,i}$  is a consequence of the limited signal to noise ratio (SNR) during the measurement of individual data points and therefore depends on the number of averages  $N_{avg}$  used in the experiments. As shown in Fig. 3e, the experimentally measured decline of  $\sigma_{R,i}$  is well fitted by  $a_i/\sqrt{N_{avg}} + c_i$  (see also Supplementary Information), as expected from the shot noise limit<sup>31</sup>. In the interest of keeping the measurement time comparable to ref.<sup>18</sup>, all experiments were performed at  $N_{avg} = 3000$ , fixing the errors at around  $\sigma/2\pi = 10$  kHz, see Fig. 3d. On average, this amounts to a relative uncertainty for the amplitude and frequency of  $\Delta A_F/A_F = 4\%$  and  $\Delta\omega_F/\omega_F = 0.5\%$ , respectively. This error increases for higher frequencies, as  $\Delta_i$  decreases for large detuning between microwave field and qudit, while the magnitude of  $\sigma_{R,i}$  remains unchanged.

Another potential source of noise, which has not been considered in the calculation above, are temporal fluctuations of the qudit transition frequencies  $\Delta_i$  due to unstable two-level systems (TLS)<sup>32–35</sup>. To quantitatively estimate their influence, we theoretically study the following example, where the first

transition frequency is shifting by  $\Delta\omega_1 = 20$  kHz<sup>34</sup> right before a sensor measurement. Then, subsequent  $\pi/2$ -pulses are even further detuned and the corresponding Ramsey frequency will be altered, resulting in an offset for  $\Delta_1$  by  $\pm\Delta\omega_1$ . Processing this offset together with the presented measurement data, we find that this causes an uncertainty for the extracted frequencies of  $\Delta\omega_F/2\pi = 16.8$  MHz. Note that this uncertainty is independent from our evaluation of  $\sigma_{R,i}$  as the shift of the transition frequency affects all data points equally. This rough estimation thus provides a reasonable explanation for the few data points, where the discrepancies  $\delta$  between  $\omega_{F,ex}$  and  $\omega_{F,apl}$  exceeding the estimated error bars in Fig. 3b. While a more profound analysis of this effect is challenging due to the varying timescales on which these fluctuations can occur, their influence could be mitigated in future measurements by a continuous recalibration of the qudit transition frequencies, i.e. adjusting the drive frequency to the fluctuating qudit transition frequencies.

In the following, we address the limits of our sensor (see Supplementary Information for an extended analysis). As discussed in ref.<sup>18</sup>, it is practical to limit the ac Stark qudit sensor to fields that are higher in frequency than the first qudit transition. Otherwise, the microwave field is more likely to excite higher qudit states. In this work, using Ramsey fringes results in additional constrains for the range of the sensor. The three

parameters defining the total measurement time for a Ramsey experiment are the maximum delay time between the  $\pi/2$ -pulses  $\Delta t_{\max}$ , the number of time steps  $N_R$  and the passive reset time  $T_{\text{rep}}$ . To reduce the measurement time together with the chance of encountering frequency fluctuation<sup>34</sup>, it is desirable to minimize these parameters. At the same time, the sampling rate  $f = N_R/\Delta t_{\max}$  should be large enough to resolve the Ramsey oscillations clearly. Here, we find that values more than five times larger than the minimum value stated by the Nyquist-Shannon theorem<sup>36,37</sup> yield accurate fits. To ensure correct fitting of the data, it is also desirable to represent at least one full oscillation period within the measurement interval, which requires a sufficiently large  $\Delta t_{\max}$ .

When operating the sensor with gate pulses that are on resonance with the unperturbed qudit frequency, Eq. (2) simplifies to  $\Delta_j = \omega_{R,j}$  and we can write the limits for the detectable frequency shifts as

$$\begin{aligned} \Delta_1/2\pi < N_R/(5 \cdot 2\Delta t_{\max}) &= 10 \text{ MHz} \\ \Delta_2/2\pi > 1/(\Delta t_{\max}) &= 1.25 \text{ MHz}, \end{aligned} \quad (3)$$

for  $N_R = 80$  and  $\Delta t_{\max} = 800 \text{ ns}$ . Together with  $T_{\text{rep}} = 240 \mu\text{s}$  and  $N_{\text{avg}} = 3000$ , all parameters amount to a total measurement time of  $\sim 1 \text{ min}$ . Note that the lower limit in Eq. (3) is given by  $\Delta_2$ , which is always a stronger constraint than  $\Delta_1$ . The lookup table in Fig. 2 visualizes the set of detectable microwave fields determined by these limits. When a different range is required, they can be adjusted by choosing  $\omega_{G,j} \neq \omega_j$  or by changing the Ramsey parameters.

## DISCUSSION

We have successfully implemented a sensor for microwave fields based on time-resolved measurements of the ac Stark shift. Employing Ramsey fringes, we harness the high sensitivity of the qudit phase on the frequencies of the first and second qudit transition. Evaluating the measured shifts with numerically generated lookup tables yields the amplitude and frequency of the applied microwave field. Using this sensing scheme, we measure the amplitude of the transfer function over a range of several hundreds of MHz. The results were validated by comparing the frequencies of the applied microwave tone with the sensor output. In comparison to the previous implementation by Schneider et al.<sup>18</sup>, we were able to increase the precision by an order of magnitude to  $\overline{\Delta A_F}/2\pi = 3.4 \text{ MHz}$  and  $\overline{\Delta \omega_F}/2\pi = 25 \text{ MHz}$  for comparable measurement times. While a full pulse calibration requires similar measurements for the phase of the transfer function (see Supplementary Information for theoretical considerations), our results may already prove useful for advancing the control over hybrid microwave systems<sup>38</sup> and could enable broadband microwave detection in superconducting particle detectors<sup>39,40</sup>.

In the future, employing parametric amplifiers<sup>41–43</sup> and active reset<sup>44–46</sup> could reduce the measurement time of the sensor to a few seconds while simultaneously improving the precision. Moreover, advanced quantum sensing protocols that use linear slope detection over an extended dynamic range can be used to further increase the precision<sup>47–49</sup>.

## METHODS

### Experimental setup

We use a standard cQED setup consisting of a transmon qudit ( $\omega_1/2\pi = 4.685 \text{ GHz}$  and  $\omega_2/2\pi = 4.405 \text{ GHz}$ ) capacitively coupled to a  $\lambda/2$ -wavelength coplanar waveguide resonator ( $\omega_r/2\pi = 6.878 \text{ GHz}$ ). To fabricate the resonator and the large-scale components of the transmon, thin-film NbTiN is used, whereas the Josephson tunnel junction consists of a conventional Al/AIO<sub>x</sub>/Al stack<sup>50</sup>. The chip is placed in a copper sample

box and cooled down to temperatures below 25mK in a wet dilution refrigerator.

The microwave gate pulses for the Ramsey sequence are generated in a single-sideband mixing scheme, using local oscillators and arbitrary waveform generators (AWG). Combined with the permanent microwave tone generating the on-chip field, these pulses are repeatedly attenuated on different temperature stages of the cryostat before reaching the sample. We use the resonator to dispersively readout the state of the qudit<sup>51,52</sup>. The readout signal is downconverted, digitized, and interpreted by our measurement software.

### Lookup table calculations

Based on the full system Hamiltonian in Eq. (1), we perform master-equation simulations using the QuTip package<sup>53,54</sup>. Starting with the transmon in the ground (excited) state  $|0\rangle$  ( $|1\rangle$ ), we compute the full time evolution while applying a Ramsey sequence by temporarily switching on  $A_G(t)$  in the simulation. After computing each point of the Ramsey fringes,  $\Delta_1$  ( $\Delta_2$ ) is determined by fitting the oscillations. This process is repeated for varying field amplitudes  $A_F$  and frequencies  $\omega_F$ , gradually filling the lookup table.

### DATA AVAILABILITY

The data that support the findings of this study is available from the corresponding author upon reasonable request.

### CODE AVAILABILITY

All data acquisition and analysis are performed with the open source measurement suite qkit (<https://www.github.com/qkitgroup/qkitgit.io/qkit>). The code used for the generation of the lookup tables is available from the corresponding author upon reasonable request.

Received: 28 October 2019; Accepted: 21 May 2020;

Published online: 25 June 2020

## REFERENCES

- Wang, D. S., Fowler, A. G. & Hollenberg, L. C. L. Surface code quantum computing with error rates over 1%. *Phys. Rev. A* **83**, 020302 (2011).
- Fowler, A. G., Mariantoni, M., Martinis, J. M. & Cleland, A. N. Surface codes: Towards practical large-scale quantum computation. *Phys. Rev. A* **86**, 032324 (2012).
- Campbell, E. T., Terhal, B. M. & Vuillot, C. Roads towards fault-tolerant universal quantum computation. *Nature* **549**, 172–179 (2017).
- Neill, C. et al. A blueprint for demonstrating quantum supremacy with superconducting qubits. *Science* **360**, 195–199 (2018).
- Chow, J. M. et al. Universal quantum gate set approaching fault-tolerant thresholds with superconducting qubits. *Phys. Rev. Lett.* **109**, 060501 (2012).
- Gustavsson, S. et al. Improving quantum gate fidelities by using a qubit to measure microwave pulse distortions. *Phys. Rev. Lett.* **110**, 040502 (2013).
- Bylander, J. et al. Pulse imaging and nonadiabatic control of solid-state artificial atoms. *Phys. Rev. B* **80**, 220506 (2009).
- Bukov, M. et al. Reinforcement learning in different phases of quantum control. *Phys. Rev. X* **8**, 031086 (2018).
- Fösel, T., Tighineanu, P., Weiss, T. & Marquardt, F. Reinforcement learning with neural networks for quantum feedback. *Phys. Rev. X* **8**, 031084 (2018).
- Niu, M. Y., Boixo, S., Smelyanskiy, V. N. & Neven, H. Universal quantum control through deep reinforcement learning. *npj Quantum Inf.* **5**, 33 (2019).
- Degen, C. L., Reinhard, F. & Cappellaro, P. Quantum sensing. *Rev. Mod. Phys.* **89**, 1–39 (2017).
- Bal, M., Deng, C., Orgiazzi, J. L., Ong, F. R. & Lupascu, A. Ultrasensitive magnetic field detection using a single artificial atom. *Nat. Commun.* **3**, 1–8 (2012).
- Hönigl-Decrinis, T., Shaikhaidarov, R., De Graaf, S. E., Antonov, V. N. & Astafiev, O. V. Two-Level System as a Quantum Sensor for Absolute Calibration of Power. *Phys. Rev. Appl.* **13**, 024066 (2020).
- Hoi, I.-C. et al. Giant Cross-Kerr effect for propagating microwaves induced by an artificial atom. *Phys. Rev. Lett.* **111**, 053601 (2013).
- Joas, T., Waeber, A. M., Braunbeck, G. & Reinhard, F. Quantum sensing of weak radio-frequency signals by pulsed Mollow absorption spectroscopy. *Nat. Commun.* **8**, 1–6 (2017).

16. Abdumalikov, A. A. et al. Electromagnetically induced transparency on a single artificial atom. *Phys. Rev. Lett.* **104**, 193601 (2010).
17. Jerger, M., Kulikov, A., Vasselin, Z. & Fedorov, A. In situ characterization of qubit control lines: a qubit as a vector network analyzer. *Phys. Rev. Lett.* **123**, 150501 (2019).
18. Schneider, A. et al. Local sensing with the multilevel ac Stark effect. *Phys. Rev. A* **97**, 062334 (2018).
19. Braumüller, J. et al. Multiphoton dressing of an anharmonic superconducting many-level quantum circuit. *Phys. Rev. B* **91**, 054523 (2015).
20. Deppe, F. et al. Two-photon probe of the Jaynes-Cummings model and controlled symmetry breaking in circuit QED. *Nat. Phys.* **4**, 686–691 (2008).
21. Astafiev, O. et al. Resonance fluorescence of a single artificial atom. *Science* **327**, 840–3 (2010).
22. You, J. Q. & Nori, F. Atomic physics and quantum optics using superconducting circuits. *Nature* **474**, 589–597 (2011).
23. Bozyigit, D. et al. Antibunching of microwave-frequency photons observed in correlation measurements using linear detectors. *Nat. Phys.* **7**, 154–158 (2011).
24. Menzel, E. P. et al. Path entanglement of continuous-variable quantum microwaves. *Phys. Rev. Lett.* **109**, 250502 (2012).
25. Dmitriev, A. Y., Shaikhaidarov, R., Antonov, V. N., Hönlgl-Decrinis, T. & Astafiev, O. V. Quantum wave mixing and visualisation of coherent and superposed photonic states in a waveguide. *Nat. Commun.* **8**, 1352 (2017).
26. Braumüller, J. et al. Concentric transmon qubit featuring fast tunability and an anisotropic magnetic dipole moment. *Appl. Phys. Lett.* **108**, 032601 (2016).
27. Koch, J. et al. Charge-insensitive qubit design derived from the Cooper pair box. *Phys. Rev. A* **76**, 1–19 (2007).
28. Lee, H., Kok, P. & Dowling, J. P. A quantum Rosetta stone for interferometry. *J. Mod. Opt.* **49**, 2325–2338 (2002).
29. Taylor, J. M. et al. High-sensitivity diamond magnetometer with nanoscale resolution. *Nat. Phys.* **4**, 810–816 (2008).
30. Peterer, M. J. et al. Coherence and decay of higher energy levels of a superconducting transmon qubit. *Phys. Rev. Lett.* **114**, 1–11 (2014).
31. Blanter, Y. & Büttiker, M. Shot noise in mesoscopic conductors. *Phys. Rep.* **336**, 1–166 (2000).
32. Lisenfeld, J. et al. Observation of directly interacting coherent two-level systems in an amorphous material. *Nat. Commun.* **6**, 1–6 (2015).
33. Klimov, P. V. et al. Fluctuations of energy-relaxation times in superconducting qubits. *Phys. Rev. Lett.* **121**, 090502 (2018).
34. Schlör, S. et al. Correlating decoherence in transmon qubits: low frequency noise by single fluctuators. *Phys. Rev. Lett.* **123**, 190502 (2019).
35. Burnett, J. J. et al. Decoherence benchmarking of superconducting qubits. *npj Quantum Inf.* **5**, 54 (2019).
36. Nyquist, H. Certain topics in telegraph transmission theory. *Trans. Am. Inst. Electr. Eng.* **47**, 617–644 (1928).
37. Shannon, C. Communication in the presence of noise. *Proc. IRE* **37**, 10–21 (1949).
38. Xiang, Z. L., Ashhab, S., You, J. Q. & Nori, F. Hybrid quantum circuits: Superconducting circuits interacting with other quantum systems. *Rev. Mod. Phys.* **85**, 623–653 (2013).
39. Booth, N. E. & Goldie, D. J. Superconducting particle detectors. *Supercond. Sci. Technol.* **9**, 493 (1996).
40. Shokair, T. M. et al. Future directions in the microwave cavity search for dark matter axions. *Int. J. Mod. Phys. A* **29**, 1443004 (2014).
41. Castellanos-Beltran, M. A., Irwin, K. D., Hilton, G. C., Vale, L. R. & Lehnert, K. W. Amplification and squeezing of quantum noise with a tunable Josephson metamaterial. *Nat. Phys.* **4**, 929–931 (2008).
42. Zhou, X. et al. High-gain weakly nonlinear flux-modulated Josephson parametric amplifier using a SQUID array. *Phys. Rev. B* **89**, 214517 (2014).
43. Winkel, P. et al. Nondegenerate parametric amplifiers based on dispersion-engineered Josephson-junction arrays. *Phys. Rev. Appl.* **13**, 024015 (2020).
44. Egger, D. et al. Pulsed reset protocol for fixed-frequency superconducting qubits. *Phys. Rev. Appl.* **10**, 044030 (2018).
45. Magnard, P. et al. Fast and unconditional all-microwave reset of a superconducting qubit. *Phys. Rev. Lett.* **121**, 060502 (2018).
46. Gebauer, R. et al. State preparation of a fluxonium qubit with feedback from a custom FPGA-based platform. Preprint at <http://arxiv.org/abs/1912.06814> (2019).
47. Berry, D. W. et al. How to perform the most accurate possible phase measurements. *Phys. Rev. A* **80**, 052114 (2009).
48. Cappellaro, P. Spin-bath narrowing with adaptive parameter estimation. *Phys. Rev. A* **85**, 030301 (2012).
49. Danilin, S. et al. Quantum-enhanced magnetometry by phase estimation algorithms with a single artificial atom. *npj Quantum Inf.* **4**, 29 (2018).
50. Wu, X. et al. Overlap junctions for high coherence superconducting qubits. *Appl. Phys. Lett.* **111**, 032602 (2017).
51. Bianchetti, R. et al. Dynamics of dispersive single-qubit readout in circuit quantum electrodynamics. *Phys. Rev. A* **80**, 043840 (2009).
52. Wallraff, A. et al. Strong coupling of a single photon to a superconducting qubit using circuit quantum electrodynamics. *Nature* **431**, 162–167 (2004).
53. Johansson, J., Nation, P. & Nori, F. QuTiP: an open-source Python framework for the dynamics of open quantum systems. *Comput. Phys. Commun.* **183**, 1760–1772 (2012).
54. Johansson, J., Nation, P. & Nori, F. QuTiP 2: a Python framework for the dynamics of open quantum systems. *Comput. Phys. Commun.* **184**, 1234–1240 (2013).

## ACKNOWLEDGEMENTS

The authors thank J. Brehm, S. Schlör, J. I. Park and M. Vissers for their feedback and helpful discussions. This work was supported by the European Research Council (ERC) under the Grant Agreement No. 648011, Deutsche Forschungsgemeinschaft (DFG) projects INST 121384/138-1FUGG and WE 4359-7, the Initiative and Networking Fund of the Helmholtz Association, and the state of Baden-Württemberg through bwHPC. A.Sch. acknowledges financial support by the Carl-Zeiss-Foundation, A. St. by the Landesgraduiertenförderung (LGF) of the federal state Baden-Württemberg and T.W. by the Helmholtz International Research School for Teratronics (HIRST). A.V.U. acknowledges partial support from the Ministry of Education and Science of the Russian Federation in the framework of Contracts No. K2-2016-063 and No. K2-2017-081.

## AUTHOR CONTRIBUTIONS

M.K. performed the measurements with support by A.Sch., A.St. and T.W. H.S.K., J.L. and D.P.P. designed and X.W. and R.L. fabricated the sample. M.K. carried out the data analysis with contributions from A.Sch. and S.D. M.K. wrote the manuscript with input from all co-authors. A.V.U. and M.W. supervised the project.

## COMPETING INTERESTS

The authors declare no competing interests.

## ADDITIONAL INFORMATION

**Supplementary information** is available for this paper at <https://doi.org/10.1038/s41534-020-00287-w>.

**Correspondence** and requests for materials should be addressed to M.K. or M.W.

**Reprints and permission information** is available at <http://www.nature.com/reprints>

**Publisher's note** Springer Nature remains neutral with regard to jurisdictional claims in published maps and institutional affiliations.



**Open Access** This article is licensed under a Creative Commons Attribution 4.0 International License, which permits use, sharing, adaptation, distribution and reproduction in any medium or format, as long as you give appropriate credit to the original author(s) and the source, provide a link to the Creative Commons license, and indicate if changes were made. The images or other third party material in this article are included in the article's Creative Commons license, unless indicated otherwise in a credit line to the material. If material is not included in the article's Creative Commons license and your intended use is not permitted by statutory regulation or exceeds the permitted use, you will need to obtain permission directly from the copyright holder. To view a copy of this license, visit <http://creativecommons.org/licenses/by/4.0/>.

© The Author(s) 2020